

# Simultaneously-Measured Mid-Infrared Refractive Indices of GaAs/AlGaAs

Lukas W. Perner,<sup>1,2,\*</sup> Gar-Wing Truong,<sup>3</sup> David Follman,<sup>3</sup> Maximilian Prinz,<sup>1</sup>  
Georg Winkler,<sup>1</sup> Stephan Puchegger,<sup>4</sup> Garrett D. Cole,<sup>3</sup> and Oliver H. Heckl<sup>1</sup>

<sup>1</sup>*Christian Doppler Laboratory for Mid-IR Spectroscopy and Semiconductor Optics,  
Faculty Center for Nano Structure Research,  
Faculty of Physics, University of Vienna,  
Boltzmannngasse 5, 1090 Vienna, Austria.*

<sup>2</sup>*Vienna Doctoral School in Physics, University of Vienna,  
Boltzmannngasse 5, 1090 Vienna, Austria.*

<sup>3</sup>*Thorlabs Crystalline Solutions, 114 E Haley St.,  
Suite G, Santa Barbara, California 93101, USA*

<sup>4</sup>*Faculty Center for Nano Structure Research,  
Faculty of Physics, University of Vienna,  
Boltzmannngasse 5, 1090 Vienna, Austria.*

(Dated: January 23, 2023)

# Abstract

We present our results for a simultaneous measurement of the refractive indices of Gallium Arsenide (GaAs) and Aluminum Gallium Arsenide ( $\text{Al}_x\text{Ga}_{1-x}\text{As}$ ) in the spectral region from  $2.0\ \mu\text{m}$  to  $7.1\ \mu\text{m}$  ( $5000\ \text{cm}^{-1}$  to  $1400\ \text{cm}^{-1}$ ). These values are obtained from a monocrystalline thin-film multilayer Bragg mirror of excellent purity (background doping  $\leq 1 \times 10^{-14}\ \text{cm}^{-3}$ ), grown via molecular beam epitaxy. To recover the refractive indices over such a broad wavelength range, we fit a dispersion model for each material. For that, we measure both a photometrically accurate transmittance spectrum of the Bragg mirror via Fourier-transform infrared spectrometry and the individual physical layer thicknesses of the structure via scanning electron microscopy. To infer the uncertainty of the refractive index values, we estimate relevant measurement uncertainties and propagate them via a Monte-Carlo-type method. This method conclusively yields propagated relative uncertainties on the order of  $10^{-4}$  over the measured spectral range for both GaAs and  $\text{Al}_{0.929}\text{Ga}_{0.071}\text{As}$ . The fitted model can also approximate the refractive index for MBE-grown  $\text{Al}_x\text{Ga}_{1-x}\text{As}$  for  $0 \leq x \leq 1$ . These updated values will be essential in the design and fabrication of next-generation active and passive optical devices in a spectral region which is of high interest in many fields, e.g., laser design and cavity-enhanced spectroscopy.

## I. INTRODUCTION

Heterostructures based on Gallium Arsenide (GaAs) and Aluminium Gallium Arsenide ( $\text{Al}_x\text{Ga}_{1-x}\text{As}$ , where  $x$  denotes the AlAs mole fraction) are widely used for active and passive (electro-)optical devices in the near-infrared (NIR) and mid-infrared (MIR) wavelength range. Among active devices are both light sources, such as vertical-cavity surface-emitting lasers (VCSELs) [1], superluminescent diodes [2] and quantum cascade lasers (QCLs) [3], as well as detection devices, such as quantum cascade detectors (QCDs) and quantum well infrared photodetectors (QWIPs) [4], and megapixel MIR camera sensors based on the QWIP technology [5]. Owing to mature fabrication technologies, notably molecular beam epitaxy (MBE) [6], GaAs/ $\text{Al}_x\text{Ga}_{1-x}\text{As}$  is also used to fabricate passive optical devices. The material system is used to deposit monocrystalline multilayers on GaAs seed wafers in order to produce thin-film interference structures, such as highly-reflective (HR) distributed Bragg

\* lukas.perner@univie.ac.at

reflectors (DBRs) [7–9]. Based on these heterostructures, so-called semiconductor saturable absorber mirrors (SESAMs) were developed to achieve modelocking in NIR lasers [10, 11] and GaAs/Al<sub>x</sub>Ga<sub>1-x</sub>As structures were successfully used in the fabrication of HR optomechanical resonators [12]. Furthermore, a recently-developed substrate-transfer technology allows the integration of GaAs/Al<sub>x</sub>Ga<sub>1-x</sub>As-based HR DBRs with curved optical substrates, making the material system relevant for applications from gravitational wave detection [13] to ultra-narrow linewidth laser stabilisation in the NIR [14]. More recently, this substrate-transfer method was extended to the MIR wavelength range [15–17], enabling ultra-low excess loss at MIR wavelengths up to 4.5 μm, making substrate-transferred GaAs/Al<sub>x</sub>Ga<sub>1-x</sub>As-based DBRs a key technology for advances in cavity-enhanced mid-infrared spectroscopy applications [18, 19].

In contrast to this wide range of applications and advances, there is a lack of recent accurate and precise data for the optical properties of GaAs/Al<sub>x</sub>Ga<sub>1-x</sub>As in the MIR wavelength range (>2 μm), especially for MBE-grown thin films. Among the most important of these optical properties is the refractive index  $n$ , which needs to be accurately known to predict the performance of both active and passive optical devices, e.g. the center wavelength (CWL), reflectance  $R$  and transmittance  $T$  of DBRs. While an extensive amount of literature values for both materials exist, much of this characterization work was done on bulk samples rather than MBE-grown multilayers. Characterization of such samples, paired with often incomplete reporting of their material properties, can lead to a significant difference in refractive index [20], especially when comparing samples grown by different methods. This constitutes a need for updated literature values for GaAs and Al<sub>x</sub>Ga<sub>1-x</sub>As, as well as other materials [21].

These differences in growth, and the associated variations in background doping and purity levels, are a likely explanation for the observed variation in MIR refractive index values (see Fig. 5) [20], thus requiring updated measurements for both materials. Especially for Al<sub>x</sub>Ga<sub>1-x</sub>As, which is used with a wide variety of mole fractions  $x$ , the latest semi-empirical model that allows for an arbitrary  $x$  was published in 1974 [22], where model parameters were obtained from a fit to measurement data obtained in the NIR range (approx. from 680 nm to 1030 nm) on samples grown via liquid-phase epitaxy (LPE) [23]. More recent studies for GaAs and Al<sub>x</sub>Ga<sub>1-x</sub>As exist [24–26]. However, these either focus on the NIR spectral region or are of insufficient accuracy for many of the above applications, which

rely on MBE-grown GaAs/Al<sub>x</sub>Ga<sub>1-x</sub>As due to discrepancies in measurement conditions and sample material (e.g., when using  $n$  measured for bulk material in the design of thin film heterostructures).

Here, we present updated refractive index values for high-purity MBE-grown GaAs and Al<sub>x</sub>Ga<sub>1-x</sub>As in the spectral range from 2 μm to 7.1 μm, measured simultaneously via a novel and robust method (this method is described in [27]), based on two widely-available measurement devices, a Fourier-transform infrared (FTIR) spectrometer and a field-emission scanning electron microscope (SEM). With those, we probe a state-of-the-art GaAs/Al<sub>x</sub>Ga<sub>1-x</sub>As DBR with a CWL of approx. 4.45 μm, recently shown to have ultra-low absorption and background doping [16, 17]. Their high purity and excellent optical properties make these DBRs, normally used to produce crystalline supermirrors [14–17], an ideal specimen to probe optical properties of the constituent materials. These measurements are then used to infer both refractive indices via a curve fitting routine based on the transmission matrix method (TMM), where the dispersive properties are captured by a semi-empirical model [22]. The measurement uncertainties are propagated to the final results for  $n$  with a Monte-Carlo-type method.

## II. MODEL, METHOD, AND THEORY

### A. Transmission Matrix Method

A well-established means of modelling the optical response (Reflectance  $R$  and/or Transmittance  $T$ ) of an optical multilayer structure is the TMM [28]. In this approach, each interface and propagation through a material with refractive index  $n$  is represented as a  $2 \times 2$ -matrix [28], effectively relating the reflected/transmitted wave to the incoming wave via the complex reflection/transmission amplitude coefficients. The TMM calculates the optical response of a multilayer based on the individual physical layer thicknesses  $d_i$  and their respective refractive indices  $n_i$ .

In principle, the TMM can incorporate absorbance within the layers via the complex refractive index  $\eta = n + i\kappa$ , with the extinction coefficient  $\kappa = \lambda_0\alpha/4\pi$  and  $\alpha$  the absorption coefficient. However, previous studies have shown that the total expected absorbance of our structure is <10 ppm (i.e.,  $< 10 \times 10^{-6}$ ) [15–17], which is below both the observed uncer-

tainty in FTIR imaging (see Fig. 1b) as well as our targeted propagated relative uncertainty of  $\sim 10^{-4}$ . Hence, we model both materials as transparent (i.e., with  $\kappa = 0$ ).

As the TMM involves matrix multiplications, numerical calculations based on the method can be implemented very efficiently. We used the recently-developed `tmm-fast` package [29], implemented in Python 3. This highly-optimized implementation allows for low computation times, even when many repeated calculations are necessary, as is the case for the employed non-linear least-squares curve fitting routines. To allow treatment of thick layers in which interference can be neglected (in our case, the MBE seed wafer), we adapted the `tmm-fast` algorithm based on the method by [28].

## B. Refractive Index Model

As our method involves a non-linear least-squares fit over a broad wavelength range (2  $\mu\text{m}$  to 7.1  $\mu\text{m}$ ), dispersion, i.e., the change of the refractive index with respect to wavelength,  $dn/d\lambda$ , must be taken into account. In principle, several different approaches to modeling refractive indices exist, roughly divided into empirical, semi-empirical, and theoretical models. The choice of an appropriate model depends on several considerations, involving the electronic and optical properties of the material in the wavelength range of interest.

For GaAs/ $\text{Al}_x\text{Ga}_{1-x}\text{As}$ , several other models have been used to obtain  $n(\lambda)$ . Empirical models are predominantly derived from the well-known Sellmeier equation [30]. The latter was used, e.g., by Skauli et al., together with another model by Pikhtin and Yas'kov, to obtain the refractive index of GaAs in a range 0.97  $\mu\text{m}$  to 17  $\mu\text{m}$  [24]. Owing to a high number of free parameters (e.g., 7 parameters per material in the case of both models in [24]), these models can capture variations in measurement data well. While this is generally desired, there is a potential for overfitting, as many free parameters allow for the model fit to extract residual random and/or systematic variations in the data points used for regression analysis.

In this study, we use a semi-empirical model developed specifically for GaAs and  $\text{Al}_x\text{Ga}_{1-x}\text{As}$  [22], given by the expression

$$n^2(E) - 1 = \frac{\eta}{\pi} \left[ \frac{E_f^4 - E_\Gamma^4}{2} + (E_f^2 - E_\Gamma^2) E^2 + \ln \left( \frac{E_f^2 - E^2}{E_\Gamma^2 - E^2} \right) E^4 \right] \quad (1)$$

where  $E = hc/\lambda$  is the photon energy,  $E_\Gamma$  is the band gap energy.  $E_f$  and  $\eta$  are to be determined empirically, effectively approximating the interband optical transitions as a function  $\epsilon_2 = \eta E^4$  for  $E_\Gamma < E < E_f$  ( $\epsilon_2 = 0$  otherwise). The lowest direct band gap energy for pure GaAs and AlAs are given by  $E_{\Gamma,\text{GaAs}} = 1.424(1)$  eV (measured at a temperature of 297 K) [20] and  $E_{\Gamma,\text{AlAs}} = 3.018$  eV (measured at room temperature, given without uncertainty) [31], respectively. Aspnes et al. showed that for arbitrary  $x$ ,  $E_\Gamma$  is well-approximated by

$$E_\Gamma(x) = 1.424 + 1.721x - 1.437x^2 + 1.310x^3 \quad (2)$$

which allows us to determine  $E_\Gamma(x)$  based on an independent measurement of  $x$ . As shown in [22], the expression in (1) closely reproduced the refractive index of GaAs for wavelengths from 0.895  $\mu\text{m}$  to 1.7  $\mu\text{m}$ , with similar results for AlAs.

To avoid bias due to model selection, we compare these results to a fit using the so-called Single Effective Oscillator (SEO) model [32], which, while not suited for the NIR, approximates  $n$  exceptionally well for  $E \ll E_{\Gamma,\text{GaAs}}$  ( $\lambda \geq 2 \mu\text{m}$ ) [22, 25]. According to this model [32], the refractive index  $n$  of a crystalline material at a photon energy  $E$  far below the bandgap is well approximated by

$$n^2(E) - 1 = \frac{E_0 E_d}{E_0^2 - E^2} \quad (3)$$

This approximates the interband optical transitions as a single dipole transition at energy  $E_0$ , with an effective oscillator strength of  $\pi E_d/2$ . Hence, the dispersion of GaAs/ $\text{Al}_x\text{Ga}_{1-x}\text{As}$  in the MIR range can be adequately modelled fitting only two free parameters,  $E_0$  and  $E_d$ , as was previously shown in [25].

### C. Monte Carlo Error Propagation

Propagation of the measured uncertainties to the best-fit model parameters is realized via a Monte-Carlo-type routine. This approach is robust to common systematic measurement errors, as the refractive indices are tightly constrained by the measured quantities.

For the purpose of uncertainty propagation, the model can be described as a function

$$T = \text{TMM}(d_i, n_{\text{Subst}}, n_{\text{GaAs}}, n_{\text{AlGaAs}}) \quad (4)$$

denoting the transmittance  $T$  as a function of the layer thicknesses  $d_i$  and refractive indices  $n$ . The fitted parameters  $n_{\text{GaAs}}$  and  $n_{\text{AlGaAs}}$  are described according to Eqs. (1–3). Here,

$T$ ,  $d_i$ , and  $n_{\text{Subst}}$  represent measured quantities with associated uncertainties. Hence, our method involves using measured quantities not only in the data the model is fit to (the  $T$  measured via FTIR), but also in the parameters used to seed the model ( $d_i$  and  $n_{\text{Subst}}$ ). Since the TMM represents a complicated model function, and a non-linear least squares fit routine is used, error propagation to the best fit parameters is not straightforward and no standardized procedure exists.

To overcome this challenge, we calculate the propagated uncertainty using the following Monte-Carlo-type method: For each run, we randomly pick a certain realization of the measurement values (layer thicknesses  $d_i$  and transmittance values  $T(\lambda)$ ) from distributions based on their respective measurement uncertainties (as given in Fig. 4b and 1b). This is repeated many times, resulting in many slightly different sets of parameters that vary within the measurement uncertainties. Each of these sets is then used for the same curve fitting exercise, in which the dispersion parameters for both materials are recorded.

This results in datasets for each fit parameter that also show variation as a consequence of the uncertainty in the measurement data. Finally, for each set of parameters, the refractive index  $n(\lambda)$  is calculated for both materials. It is of note that the uncertainty in  $n$  is much smaller than what would result from Gaussian error propagation, because the fitted parameters show appreciable covariance with the input parameters taken from measurement and literature values. This is best seen when comparing the uncertainties resulting from fitting Eq. (1) vs. Eq. (3): Although the former uses literature and measurement values for  $E_T$  and  $x$  with associated additional uncertainties when compared to the latter, this leads to a negligible difference in the observed standard uncertainty of  $n$ .

### III. EXPERIMENT

The basic idea of our approach is the following: On the one hand, the optical response, in our case the transmittance  $T$ , of a transparent optical system can be accurately modelled via TMM if the physical structure (i.e., layer thicknesses) and the associated refractive indices are known. On the other hand, transmittance is accessible to optical probing. As a result, knowing both the measured optical response as well as the material composition and layer thicknesses of an optical structure allows to determine the refractive indices. This means that the refractive indices can be uniquely determined for a two-material structure which

exhibits a characteristic optical response in the wavelength range of interest.

While this work details results for GaAs/Al<sub>x</sub>Ga<sub>1-x</sub>As, the underlying measurement principle (combining knowledge of the optical response with measurements of the physical structure of a thin-film multilayer to simultaneously obtain the refractive indices of two materials) is much broader in its applicability, as is discussed in [27]. It can be adapted for different measurement devices and spectral ranges. In this study, data collection consists of two independent measurements: (i) obtaining a photometrically accurate transmittance  $T$  spectrum via Fourier-transform infrared (FTIR) spectrometry (ii) measuring individual physical layer thicknesses  $d_i$  via calibrated SEM metrology. As explained in II A, the TMM relates the optical layer thicknesses to the optical response of a layered system.

### A. Fabrication and Description of the GaAs/Al<sub>x</sub>Ga<sub>1-x</sub>As Sample

The sample under test was designed to serve as half of a distributed Bragg reflector (DBR) structure centered at  $\lambda_d = 4.5 \mu\text{m}$ . Nominally, this structure consisted of 22.5 periods of Al<sub>x</sub>Ga<sub>1-x</sub>As/GaAs layer pairs, with an optical layer thickness of  $\lambda_d/4$ , terminated by a single  $\lambda_d/8$ -thickness GaAs cap (46 layers total) to avoid exposure of Al<sub>x</sub>Ga<sub>1-x</sub>As to air, preventing oxidation. The target AlAs mole fraction in the Al<sub>x</sub>Ga<sub>1-x</sub>As layers was  $x = 0.92$ .

Based on the above design, a DBR specimen was deposited via MBE on a [001]-oriented semi-insulating (GaAs with As anti-site defects) GaAs seed wafer with a diameter of 15 cm and a nominal thickness of 675(25)  $\mu\text{m}$ . From this as-grown structure (seed wafer plus MBE-deposited heterostructure), we cleaved a rectangular die of  $2 \times 2 \text{ cm}^2$ , which served as the sample for all parts of this study. After growth, the AlAs mole fraction  $x$  was estimated to be 92.9(30) % based on a x-ray diffraction (XRD) measurement performed by the epitaxial material supplier. Here, the uncertainty represents a conservative estimate based on data from [33, 34]. In our analysis, we assume that the mole fraction  $x$  is the same for all Al<sub>x</sub>Ga<sub>1-x</sub>As layers and that interfaces between the layers are abrupt (i.e., that  $n$  changes over a distance  $\ll \lambda$ ).

Recently, a two mirror cavity using 44.5 period DBR mirrors fabricated with material from the same growth run demonstrated a Finesse of 230 000, corresponding to a per-mirror excess loss (absorption plus scatter) of 4.27(52) ppm. From this an average extinction coefficient  $k < 10^{-6}$  was extracted, suggesting background doping levels of  $\leq 10^{-14} \text{ cm}^{-3}$  [17]. This

high purity makes the multilayer structure an ideal specimen to measure the refractive index  $n$  of both materials from an optical measurement.

## B. Transmission Spectrum via Fourier-Transform Infrared Spectrometry

We obtain FTIR transmittance  $T$  spectra using a commercially available vacuum FTIR spectrometer (Bruker Vertex 80v). As described below, the necessary photometric accuracy was obtained by thorough calibration and rigorous control of measurement conditions.

### 1. Measurement Conditions and Parameters

To obtain the transmittance spectra with excellent photometric accuracy, we thoroughly characterized the FTIR device and optimized the measurement parameters. From these efforts, we find that a SiC globar-type light source with a 2 mm aperture to be optimal. The aperture size is chosen to maximize throughput while obtaining a well-collimated beam (excluding influence on resolution due to a large source diameter). A standard KBr beamsplitter was used for optimal modulation efficiency over the wavelength region of interest. The scan speed of the moving interferometer mirror is set to 10 kHz (corresponding to a physical scan speed of  $\sim 0.32 \text{ cm s}^{-1}$ ), limited by the RF-frequency bandwidth of the employed DLaTGS pyroelectric detector. This detector was chosen because of its excellent linearity and flat detectivity  $D^*(\lambda)$  over our measurement range [35, 36], minimizing systematic errors due to nonlinear detector response. Wavelength calibration of the FTIR is verified by comparing the spectrum of a polystyrene filter with a manufacturer-supplied calibration curve. All measurements are performed after evacuation (2.21 mbar). We find that optimal stability and repeatability of the above configuration is achieved  $>10$  h after starting evacuation and switching on the light source. Possible causes for this are thermalization (light source and/or detector) or a gradual improvement in evacuation. It is of note that this is well above the stabilization time recommended by the manufacturer (4 h), which we attribute to ageing of our device. Because of the relatively low detectivity of the detector and the resulting single shot signal-to-noise ratio (SNR), each individual measurement is the average of 256 individual interferograms, resulting in a measurement time of 15 min per measurement.

All measurements are recorded as double-sided interferograms. That way, the phase spec-

trum is available at the same resolution as the power spectrum for the FT process, avoiding photometric errors from phase correction of single-sided interferograms [37]. Each averaged interferogram was subsequently transformed to a spectrum with  $2\text{ cm}^{-1}$  resolution, using a Norton-Beer medium apodization and Mertz phase correction in the process, previously shown to yield optimal photometric accuracy [38]. Finally, sample measurements are ratioed against a background spectrum which was measured under identical conditions immediately before. Both sample and background measurements were repeated several times to estimate the type A uncertainties for each series over our entire measurement range  $1400\text{ cm}^{-1}$  to  $5000\text{ cm}^{-1}$  (see Fig. 1b).

The sample was held at a constant temperature of  $T_s = 22(1)^\circ\text{C}$  by a custom-built optomechanical mount using a single stage TEC element to exclude fluctuations due to thermal drift. We carefully aligned the sample to normal incidence (overlapping the reflected light with the incident beam at the entrance of the sample chamber), with an estimated error of  $<0.3^\circ$ .

The type A uncertainty of this measurement routine was estimated by repeated measurements of both the reference (sample size  $i = 14$ ) and sample ( $i = 8$ ) spectra. These measurements were subsequently ratioed to obtain the transmittance spectrum of the DBR as well as the associated uncertainty.

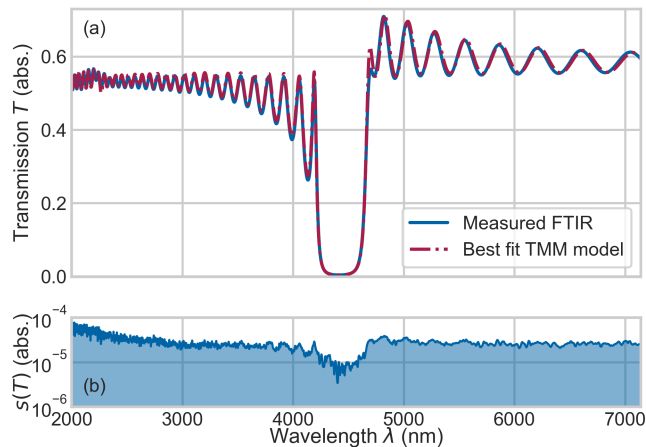


FIG. 1. (a) Transmittance spectra of the measured sample multilayer structure. As measured in FTIR (blue) and the best fit model as obtained when calculating a nonlinear least-squares regression with the TMM model based on the physical layer thicknesses as extracted from SEM. (b) Statistical  $1s$  standard uncertainty of the FTIR measurements.

## 2. Temperature-resolved measurements

The aforementioned TEC-stabilized mount also allowed us to cool/heat the sample in a limited range of 19 °C to 29 °C. Temperature stability was better than  $\pm 0.1$  K, while accuracy was limited by the thermistor (accuracy and calibration error) to  $\pm 1$  K. Temperature readings are given in Fig. 2. As discussed in [24], such temperature dependent measurements can be used to extract  $dn/dT_s$  and  $d^2n/dT_s^2$ , as the linear thermal expansion coefficient of GaAs/Al<sub>x</sub>Ga<sub>1-x</sub>As is well known [24]. Accurate extraction of these parameters would require a wider range temperatures, beyond the capabilities of our custom-built mount (designed for temperature stabilization rather than appreciable heating or cooling).

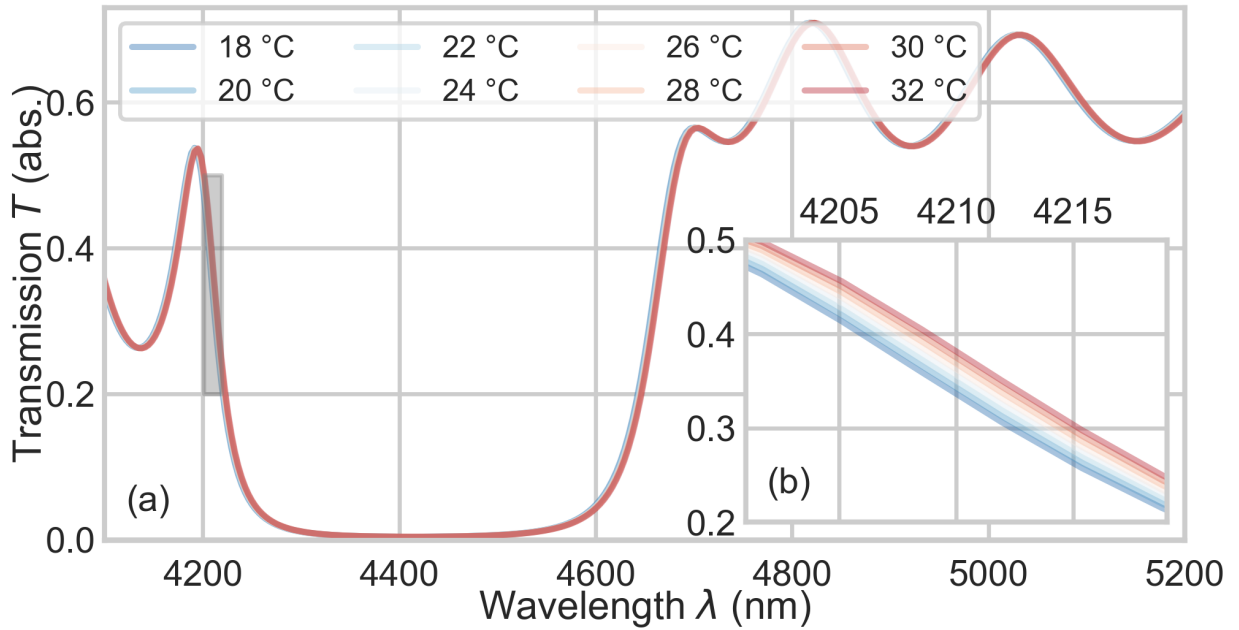


FIG. 2. (a) Temperature resolved measurements spanning 18–32 °C, including the measurement used for retrieving the refractive indices at 22 °C. (b) As systematic shifts are barely visible in the main figure, we shows a zoom of the shaded area in (a). The shift of approx. 3 nm at 4210 nm due to changes in temperature is clearly visible.

## C. Scanning Electron Microscope Measurements

The individual thickness of each GaAs/Al<sub>x</sub>Ga<sub>1-x</sub>As layer was measured using a scanning electron microscope (Zeiss Supra 55 VP) providing a cross-section of the same sample used

in FTIR measurements.

The described routine takes direct advantage of the excellent thickness uniformity of epitaxial DBRs, which was demonstrated to be less than 0.41(5) nm RMS over a 4 cm diameter round sample in [39]. This allowed for the extraction of individual measurements from several thousand high-resolution line scans to calculate sample statistics and thereby drastically reduce the standard uncertainty.

### *1. Sample Preparation*

Prior to revealing the cross section, we deposited a gold layer on top of the heterostructure using a table-top sputtering device (Leica EM SCD050 with EM QSG100 monitor) to avoid contrast issues at the air-GaAs boundary in SEM metrology (see Fig. 3). To reveal the cross-section of the multilayer, the die was cleaved within the  $\sim 2$  mm spot probed in FTIR spectrometry using a standard diamond scribe. As we used a lattice-matched monocrystalline heterostructure this results in a cross section perpendicular to the front surface (flatness was confirmed using a secondary electron detector in SEM). Finally, the sample is mounted on a  $90^\circ$  sample-holder stub to exclude systematic errors (tilt angle and vibration).

As  $\text{Al}_x\text{Ga}_{1-x}\text{As}$  is known to form oxide layers, care was taken that the sample is exposed to atmosphere prior to SEM imaging for no more than 15 min. According to prior studies [40], this will cause an oxide layer of  $\sim 1$  nm thickness for our sample. We find this to be negligible compared to the mean interaction depth of backscattered electrons, simulated to be  $\gg 1$  nm at 10 keV (using CASINO v2.51 [41]). Hence, this thin oxide film does not affect SEM imaging using a backscattered electron detector (BSD).

### *2. Cross-Sectional Measurement*

The mounted sample is loaded on the SEM's multi-sample holder together with a certified calibration standard (EM-TEC MCS-0.1CF). After evacuation of the system ( $5 \times 10^{-5}$  mbar), we performed all measurements at a beam energy of 10 keV. All images used in this evaluation were obtained at a working distance of 9.5 mm. Prior to calibration and measurement we set a nominal magnification of  $\sim 6600$ , so that the the

complete multilayer is captured in a single image. We therefore use the standard's  $1\ \mu\text{m}$  grid (17 lines with  $1\ \mu\text{m}$  pitch, certified total length of  $16.0100(48)\ \mu\text{m}$ ) to calibrate the SEM at the chosen magnification. This standard is imaged with the above settings after optimizing the stigmator and the focus to obtain a undistorted image (see Fig. 3a). Following the calibration step, we used the translation stage of the SEM to position the cross section of our heterostructure below the electron gun. In this step, we also corrected for a slight height difference between standard and sample by moving the cross section into focus (at identical working distance etc.) using the same translation stage. Having thereby achieved identical conditions compared to calibrations, the heterostructure is imaged with identical parameters as the standard at 4 distinct positions. Care is taken to avoid imaging parts of the structure twice.

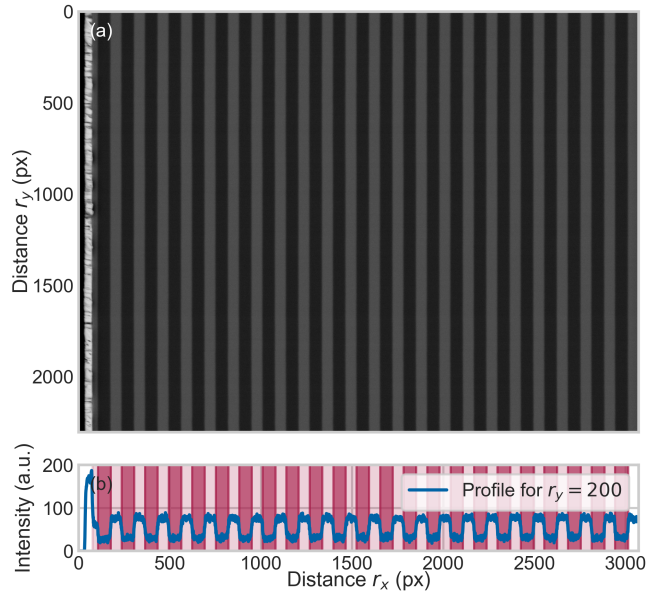


FIG. 3. (a) One of a total of four SEM images of the DBR under test. Leftmost layer is gold, coated after FTIR to exclude boundary effects in SEM metrology. (b) Typical profile of a single row (blue) with extracted layer thicknesses (red).

### 3. Evaluation

Our approach to extract the interface positions using a custom Python3 script, for both the standard and the sample, is as follows: 1. loading the picture as a 2D array, where every

entry is assigned the 8 bit grayscale value of the corresponding pixel, 2. slicing the image row-by-row to get a profile (see Fig. 3b), 3. estimating the interface positions by finding the extrema of the first derivative of the row-wise profile, 4. dividing each single row profile in smaller intervals around the estimated interface positions so that each intervals contains a single interface, 5. for each interface, fitting an error function and use the inflection point of the fitted curve as our estimate for the interface position (using the error function is justified by the fact that it is the convolution of an electron beam, approximated by a Gaussian profile, and the abrupt material interface, approximated by a step function), 6. layer thicknesses are obtained by subtracting subsequent estimates for the interface positions from each other 7. repeating the above procedure for all rows in the image, we find the mean and  $1s$  standard uncertainty of the mean for each layer  $s(d_i)$

In case of the sample, the above procedure is repeated for all four images. In this procedure, we excluded significant systematic errors due to sample tilt by testing for systematic changes of extracted interface positions.

From the evaluation of the reference standard, we establish a calibrated distance per imaged pixel. For that, we measured the certified distance (first to last line) of the standard (in pixels) to be 2844.807(10) px. This results in a calibrated pitch of 5.6278(17) nm px<sup>-1</sup>. The propagated uncertainty of 0.03 % is dominated by the certified uncertainty of the standard, as the relative statistical uncertainty is <4 ppm. These results are used to calibrate the subsequent evaluation of the sample under test.

From four SEM images of the GaAs/Al<sub>x</sub>Ga<sub>1-x</sub>As heterostructure, we extract the mean and standard uncertainty of the individual layer thicknesses in units of pixels. These values were subsequently multiplied by the calibrated pitch to obtain physical layer thicknesses in units of nanometers. The resulting mean thickness and inferred uncertainty of each individual layer is summarized in Fig. 4.

The propagated relative uncertainty ( $< 4 \times 10^{-4}$  for all  $\lambda_d/4$  layers) is dominated by the uncertainty of the calibration standard, except for the topmost  $\lambda_d/8$  GaAs layer, which exhibits a relative uncertainty of  $2.2 \times 10^{-3}$ . This is caused by the Au/GaAs interface, where the data quality suffers from remaining structure in the Au cross section that could not be eliminated.

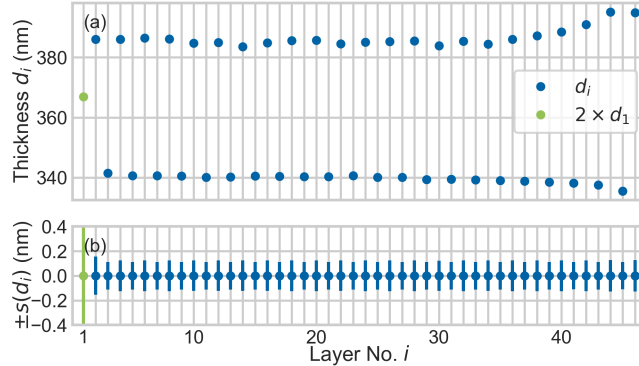


FIG. 4. (a) Measured layer thicknesses, resulting from averaging row-wise measurements. Note that the thickness of the 1/8-wave cap,  $d_1$ , (green) was multiplied by a factor of 2. (b) Error bars showing  $1s$  standard uncertainty for the mean values given in (a).

#### IV. RESULTS

To obtain the refractive indices of GaAs/ $\text{Al}_x\text{Ga}_{1-x}\text{As}$  from the above measurements, we used a non-linear least-squares fitting approach. In that process, we used a TMM model based on the layer thicknesses obtained via SEM, and model the refractive indices according to the models in Eq. (1) and (3). The resulting curve is then fitted to the photometrically-accurate FTIR transmittance  $T$  spectrum (see Fig. 1a) to obtain values for the free parameters, effectively resulting in values for the refractive indices of GaAs/ $\text{Al}_x\text{Ga}_{1-x}\text{As}$ .

To obtain accurate mean values and standard uncertainties for both refractive indices, we use the described Monte-Carlo-type uncertainty propagation. This involves running the fit routine 1000 times for each model, where each time the transmittance values  $T(\lambda)$ , the individual layer thicknesses  $d_i$ , and, in case of Eq. 1, the AlAs content  $x$  and literature values for  $E_\Gamma$ , are randomly picked from normal distributions representing their respective propagated measurement uncertainty. The resulting distributions, which give the mean and standard uncertainty for  $n$ , closely followed a normal distribution. Each set of Monte-Carlo parameters is then used to calculate the refractive index, where the variation of these calculations results in mean values and standard uncertainties for both indices  $n(\lambda)$ , which we show in Fig. 5. Model parameters reproducing our results are reported in Tab. I for ease of computation. The biggest relative standard uncertainty is observed at the lower-wavelength end of our spectrum. Using Eq. (1) with Eq. (2), these values are  $s(n_{\text{GaAs}})/n_{\text{GaAs}} \leq 3.2 \times 10^{-4}$  and  $s(n_{\text{AlGaAs}})/n_{\text{AlGaAs}} \leq 2.8 \times 10^{-4}$ , whereas uncertainties for Eq. (3) are  $\leq 3.3 \times 10^{-4}$  and

$\leq 2.9 \times 10^{-4}$  for GaAs and  $\text{Al}_{0.929}\text{Ga}_{0.071}\text{As}$ , respectively. We report these as the uncertainty for  $n$  when calculated with parameters in Tab. I over the whole wavelength range.

## V. CONCLUSION AND OUTLOOK

In summary, we report the simultaneous measurement of refractive index  $n$  values for both pure GaAs and  $\text{Al}_{0.929}\text{Ga}_{0.071}\text{As}$  in the spectral range from  $2\ \mu\text{m}$  to  $7.1\ \mu\text{m}$  at room temperature ( $T_s = 22(1)\ \text{°C}$ ). These measurements were obtained via a novel, highly adaptable method that involves probing a monocrystalline quarter-wave DBR [27], grown via MBE with exceptionally low background doping. This was achieved by acquiring a photometrically-accurate transmittance spectrum via FTIR spectrometry, as well as an accurate measurement of individual layer thicknesses via calibrated SEM metrology. For both measurements, control of systematic errors was necessary but achieved by simple means such as careful alignment and temperature stabilization.

Subsequently, we performed a non-linear least-squares fitting routine based on TMM modelling, where the dispersion  $dn/d\lambda$  was modelled according to two different models for each refractive index. Finally, the best-fit results are used to obtain the refractive indices

TABLE I. Parameters to calculate the refractive indices for both materials according to our results for models given by Eq. (1) and Eq. (3).

Material	Model	Variable	Value
GaAs	Eq. (2)	$x$	0
	Eq. (1)	$\eta$	0.170481
		$E_f$	4.36144
		Eq. (3)	$E_0$
		$E_d$	31.1845
$\text{Al}_{0.929}\text{Ga}_{0.071}\text{As}$	Eq. (2)	$x$	0.929
	Eq. (1)	$\eta$	0.0393107
		$E_f$	5.90697
		Eq. (3)	$E_0$
		$E_d$	33.4811

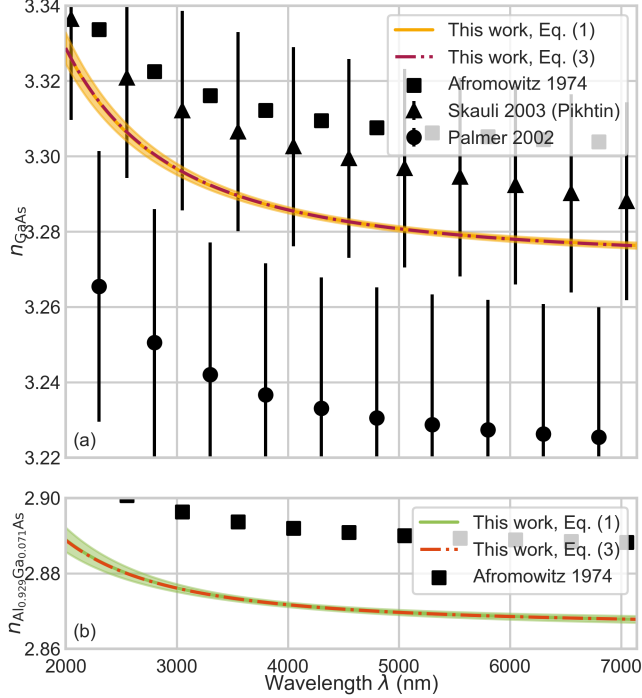


FIG. 5. Final results for the refractive indices, where error bands/bars for our results obtained from fitting Eq. (1) and for values from Skauli et al. are given as fourfold standard uncertainty  $4s(n)$ , while the error bars for Palmer et al. are given as  $1s(n)$ . Values for Afromowitz represent an extrapolation from the NIR with unknown uncertainty. Error bands for our fit of Eq. (3) are omitted because they are almost identical to those for Eq. (1). (a) Refractive index of GaAs. (b) Refractive index of  $\text{Al}_{0.929}\text{Ga}_{0.071}\text{As}$ .

for GaAs/ $\text{Al}_{0.929}\text{Ga}_{0.071}\text{As}$  over the entire wavelength range. Propagation of measurement uncertainties via a Monte-Carlo-based method suggest relative uncertainties on the order of  $10^{-4}$  for both materials.

We achieve good agreement with previously-published results. Differences to the values published in [22] are explained by the fact that this data represents an extrapolation from a fit to NIR measurements. Notably, the data by Palmer et al. [25] shows the biggest discrepancy, believed to be caused by a systematic offset due to the incorrect assumption of perfectly uniform high- and low-index layers. The discrepancy with regards to the results by Skauli et al. [24], which were used to model the GaAs wafer in the present study, are most likely due to different material properties when comparing MBE-grown GaAs with LEC/VGF-grown GaAs wafers. These are most likely caused by different free-carrier concentrations [20].

As our results were extracted from a state-of-the-art MBE-grown thin-film heterostructure, which is one of the most important use cases for GaAs and  $\text{Al}_x\text{Ga}_{1-x}\text{As}$  in the MIR wavelength range, we believe that these updated values should find use in the design of future active and passive optical devices in the MIR range.

## ACKNOWLEDGMENTS

We thank Dr. Stefan Eichler at Freiburger Compound Materials GmbH for GaAs wafer characterization data, Prof. Thomas Pichler for access to his group's FTIR device, and Dr. Adam J. Fleisher at NIST Gaithersburg for in-depth discussions and helpful advice.

We acknowledge support by the Faculty Center for Nano Structure Research at the University of Vienna, providing the SEM. The financial support by the Austrian Federal Ministry for Digital and Economic Affairs, the National Foundation for Research, Technology and Development and the Christian Doppler Research Association is gratefully acknowledged.

- 
- [1] C. W. Wilmsen, H. Temkin, and L. A. Coldren, eds., *Vertical-Cavity Surface-Emitting Lasers* (Cambridge University Press, 2001).
  - [2] C.-F. Lin and B.-L. Lee, *Applied Physics Letters* **71**, 1598 (1997).
  - [3] C. Sirtori, P. Kruck, S. Barbieri, P. Collot, J. Nagle, M. Beck, J. Faist, and U. Oesterle, *Applied Physics Letters* **73**, 3486 (1998).
  - [4] D. Hofstetter, F. R. Giorgetta, E. Baumann, Q. Yang, C. Manz, and K. Köhler, *Applied Physics B* **100**, 313 (2010).
  - [5] S. Gunapala, S. Bandara, J. Liu, C. Hill, S. Rafol, J. Mumolo, J. Trinh, M. Tidrow, and P. LeVan, *Infrared Physics & Technology* **47**, 67 (2005).
  - [6] U. W. Pohl, *Epitaxy of Semiconductors*, Graduate Texts in Physics (Springer International Publishing, Cham, 2020).
  - [7] J. P. van der Ziel and M. Ilegems, *Applied Optics* **14**, 2627 (1975).
  - [8] J. P. van der Ziel and M. Ilegems, *Applied Optics* **15**, 1256 (1976).
  - [9] W. Heiss, T. Schwarzl, J. Roither, G. Springholz, M. Aigle, H. Pascher, K. Biermann, and K. Reimann, *Progress in Quantum Electronics* **25**, 193 (2001).

- [10] U. Keller, K. Weingarten, F. Kartner, D. Kopf, B. Braun, I. Jung, R. Fluck, C. Honninger, N. Matuschek, and J. Aus der Au, *IEEE Journal of Selected Topics in Quantum Electronics* **2**, 435 (1996).
- [11] U. Keller, *Applied Physics B* **100**, 15 (2010).
- [12] G. D. Cole, S. Gröblacher, K. Gugler, S. Gigan, and M. Aspelmeyer, *Applied Physics Letters* **92**, 261108 (2008).
- [13] B. Barr, A. Bell, C. Bell, C. Bond, D. Brown, F. Brueckner, L. Carbone, K. Craig, A. Cumming, S. Danilishin, K. Dooley, A. Freise, T. Fricke, P. Fulda, S. Giampsis, N. Gordon, H. Grote, G. Hammond, J. Harms, S. Hild, J. Hough, S. Huttner, R. Kumar, H. Lück, N. Lockerbie, J. Macarthur, I. Martin, P. Murray, S. Reid, S. Rowan, D. Shoemaker, B. Sorazu, K. Strain, S. Tarabrin, K. Tokmakov, and N. Voronchev, *LIGO 3 Strawman Design, Team Red (T1200046-v1)*, Tech. Rep. (LIGO, 2012).
- [14] G. D. Cole, W. Zhang, M. J. Martin, J. Ye, and M. Aspelmeyer, *Nature Photonics* **7**, 644 (2013).
- [15] G. D. Cole, W. Zhang, B. J. Bjork, D. Follman, P. Heu, C. Deutsch, L. Sonderhouse, J. Robinson, C. Franz, A. Alexandrovski, M. Notcutt, O. H. Heckl, J. Ye, and M. Aspelmeyer, *Optica* **3**, 647 (2016).
- [16] G. Winkler, L. W. Perner, G.-W. Truong, G. Zhao, D. Bachmann, A. S. Mayer, J. Fellingner, D. Follman, P. Heu, C. Deutsch, D. M. Bailey, H. Peelaers, S. Puchegger, A. J. Fleisher, G. D. Cole, and O. H. Heckl, *Optica* **8**, 686 (2021).
- [17] G.-W. Truong, L. W. Perner, G. Winkler, S. B. Cataño-Lopez, C. Nguyen, D. Follman, O. H. Heckl, and G. D. Cole, arxiv: **2209.09902v2** (2022).
- [18] G. Gagliardi and H.-P. Loock, *Springer Series in Optical Sciences*, edited by G. Gagliardi and H.-P. Loock, Springer Series in Optical Sciences (Springer, Berlin, Heidelberg, 2014).
- [19] B. J. Bjork, T. Q. Bui, O. H. Heckl, P. B. Changala, B. Spaun, P. Heu, D. Follman, C. Deutsch, G. D. Cole, M. Aspelmeyer, M. Okumura, and J. Ye, *Science* **354**, 444 (2016).
- [20] D. D. Sell, H. C. Casey, and K. W. Wecht, *Journal of Applied Physics* **45**, 2650 (1974).
- [21] S. G. Kaplan, L. M. Hanssen, U. Griesmann, and R. Gupta, in *Proceedings of SPIE*, Vol. 3425, edited by R. V. Datla and L. M. Hanssen (1998) pp. 203–212.
- [22] M. A. Fromowitz, *Solid State Communications* **15**, 59 (1974).
- [23] H. C. Casey, D. D. Sell, and M. B. Panish, *Applied Physics Letters* **24**, 63 (1974).

- [24] T. Skauli, P. S. Kuo, K. L. Vodopyanov, T. J. Pinguet, O. Levi, L. A. Eyres, J. S. Harris, M. M. Fejer, B. Gerard, L. Becouarn, and E. Lallier, *Journal of Applied Physics* **94**, 6447 (2003).
- [25] C. Palmer, P. N. Stavrinou, M. Whitehead, and C. C. Phillips, *Semiconductor Science and Technology* **17**, 1189 (2002).
- [26] K. Papatryfonos, T. Angelova, A. Brimont, B. Reid, S. Guldin, P. R. Smith, M. Tang, K. Li, A. J. Seeds, H. Liu, and D. R. Selviah, *AIP Advances* **11**, 025327 (2021).
- [27] L. W. Perner, G.-W. Truong, D. Follman, M. Prinz, G. Winkler, S. Puchegger, G. D. Cole, and O. H. Heckl (2023), unpublished.
- [28] S. J. Byrnes, arxiv: **1603.02720** (2021).
- [29] A. Luce, A. Mahdavi, F. Marquardt, and H. Wankerl, *Journal of the Optical Society of America A* **39**, 1007 (2022).
- [30] W. v. Sellmeier, *Annalen der Physik und Chemie* **219**, 272 (1871).
- [31] H. C. H. C. Casey and M. B. Panish, *Heterostructure lasers* (Academic Press, 1978).
- [32] S. H. Wemple and M. DiDomenico, *Physical Review B* **3**, 1338 (1971).
- [33] K. Bertness, J. Armstrong, R. Marinenko, L. Robins, A. Paul, J. Pellegrino, P. Amirtharaj, and D. Chandler-Horowitz, in *2000 Digest of the LEOS Summer Topical Meetings. Electronic-Enhanced Optics. Optical Sensing in Semiconductor Manufacturing. Electro-Optics in Space. Broadband Optical Networks (Cat. No.00TH8497)* (IEEE, 2000) pp. II21–II22.
- [34] K. A. Bertness, T. E. Harvey, C.-M. Wang, A. J. Paul, and L. H. Robins, *Standard Reference Materials 2840 to 2482 Composition standards for AlGaAs epitaxial layers (NIST SP 260-163)*, Tech. Rep. (NIST, Gaithersburg, MD, 2006).
- [35] E. Theocharous and J. Birch, in *Handbook of Vibrational Spectroscopy*, edited by J. M. Chalmers (John Wiley & Sons, Ltd, Chichester, UK, 2006) pp. 1–19.
- [36] E. Theocharous, *Applied Optics* **47**, 3731 (2008).
- [37] D. B. Chase, *Applied Spectroscopy* **36**, 240 (1982).
- [38] P. R. Griffiths and J. A. de Haseth, *Fourier Transform Infrared Spectrometry*, 2nd ed., *Chemical Analysis* (Wiley, Hoboken, 2007).
- [39] P. Koch, G. D. Cole, C. Deutsch, D. Follman, P. Heu, M. Kinley-Hanlon, R. Kirchhoff, S. Leavey, J. Lehmann, P. Oppermann, A. K. Rai, Z. Tornasi, J. Wöhler, D. S. Wu, T. Zederbauer, and H. Lück, *Optics Express* **27**, 36731 (2019).

- [40] F. Reinhardt, B. Dwir, and E. Kapon, *Applied Physics Letters* **68**, 3168 (1996).
- [41] D. Drouin, A. R. Couture, D. Joly, X. Tastet, V. Aimez, and R. Gauvin, *Scanning* **29**, 92 (2007).